Structure and substructure in the stellar halo of the Milky Way

Pila Diez, B.

Chapter 3

A KiDS view on the structure of the Galactic halo

Authors

B. Pila-Díez, J.T.A. de Jong and K. Kuijken

Abstract

We study the density profile and shape of the Galactic halo using deep multi-colour images from the Kilo Degree Survey (KiDS) on the VLT Survey Telescope, in combination with previous MENeaCS and CCCP surveys to strengthen the constraining power through multiple lines of sight. The significant photometric depth and the Southern lines of sight of KiDS allow us to probe new regions of the halo. We build catalogues of near Main Sequence Turnoff point stars by homogenizing the PSF of the images, separating stars from galaxies through fixed-aperture photometry and using a multicolour selection for halo F stars. We calculate galactocentric distances for these stars and build density profiles along several lines of sight out to 60 kpc. We then add lines of sight from our earlier analysis of the MENeaCS and the CCCP surveys, and fit global halo models to the density profiles. We find that the stellar halo is best described by a power law model with a break in the power index, located within $[22, 30)$ kpc. The inner power law index is dependent on the value of the break distance ($n_{in} = [-3.30, -3.90) \pm 0.05$), whereas the outer power law index is quite stable ($n_{in} = -4.6 \pm 0.1$). We find a polar axis ratio of $q = 0.77 \pm 0.05$, in agreement with previous works, and an indication of a very mild triaxiality $w = 0.94 \pm 0.05$. We also recover data-to-model deviations matching previously known overdensities such as the Sagittarius stream and the Virgo Overdensity, and possible extensions of these or other substructures to greater distances than expected.

3.1 Introduction

Hierarchical galaxy formation is a natural consequence of the current cosmological model. Many of the oldest stars are expected to have formed in small galaxies, long before they were swallowed up into larger objects, and some are expected to have formed in-situ or evaporated from early low-mass globular clusters. Consequently, the oldest stars provide a fossil record of the beginnings of galaxy formation. Even though these stars only comprise a tiny fraction of the mass of present-day galaxies, their study is therefore worthwhile. The Galaxy is a unique environment in which to trace old stars, because stellar populations can be isolated star-by-star, even in regions where the surface brightness is well below observational limits in external galaxies.

Extensive studies of the star distribution in the Galactic outskirts have been undertaken (mostly in the Northern hemisphere) and have revealed a wealth of substructure in the form of streams and satellites—clear evidence of past accretion and merger processes (York et al. (2000); Ahn et al. (2014) and Skrutskie et al. (2006)). Also, the overall structural parameters of the stellar halo have been measured, yielding a picture of an ellipsoidal distribution with a radial density profile in the form of a broken power law. As data have improved, it has become possible to probe the halo with fainter, more abundant stars, close to the main sequence turnoff: a significant advance over older studies based on horizontal branch or red giant stars.

In this paper we use deep photometry from the Kilo Degree Survey (KiDS) obtained with the VLT Survey Telescope (VST) and its wide-field camera OmegaCAM to probe main sequence turn-off (MSTO) stars out to distances of 60 kpc. The KiDS main distinguishing attributes are both its footprint on the Southern sky and its outstanding depth, wich make it competitive in terms of the distant and faint or the otherwise uncharted halo. We split the current KiDS data into ten broad lines of sight through the Galactic halo to constrain its general stellar structure and probe potential substructure. We combine them with previous data from the Canada-France-Hawaii Telescope (CFHT) MegaCam and the Wide Field Camera (WFC) at the Isaac Newton Telescope (INT) – providing eight additional lines of sight– in order to increase its constraining power (Pila-Díez et al. 2015). In section 2 we describe the observations and the data processing relevant to our stellar catalogues and to our analysis. In section 3 we cover the star selection, the building of the density profiles and the smooth halo models that we consider. Finally, in section 4 we discuss and give context to our findings, and in section 5 we summarize our conclusions.

3.2 Survey and stellar catalogues

3.2.1 The Kilo Degree Survey

One of the Public Surveys conducted with the VLT Survey Telescope (VST), the Kilo-Degree Survey (KiDS, de Jong et al. 2013) is currently in the process

of imaging 1500 square degrees of extragalactic sky in four optical broad-band filters (u, g, r and i). The survey area is split between two fields, one in the northern and one in the southern Galactic cap. Aimed primarily at constraining the dark matter distribution in the universe through weak gravitational lensing, KiDS delivers deep and high quality images with typical image quality (PSF FWHM) ranging from $0.7''$ in r to $1.1''$ in u. KiDS limiting magnitudes are approximately 2 magnitudes fainter than those of SDSS: 24.3 in u, 25.1 in g, 24.9 in r and 23.7 in i.

The individual pointings are 1×1 deg^2. They are built up from four (u) or five (gri) dithers to fill inter-CCD gaps, with each position visited once for each filter, yielding the final survey depth in one go. During the first years of operation, the Galaxy And Mass Assembly (GAMA, Driver et al. 2011) fields have been prioritized to maximize the synergy with these deep spectroscopic data.

The KiDS data used in this work are from the first and second public data releases. Figure 3.1 shows the location of the included fields on the sky and the planned final coverage. A detailed description of the data reduction is provided in the release notes or on the KiDS website[1], but here follows a brief summary. Following cross-talk correction, satellite track removal and flat-fielding, an illumination correction is applied in order to flatten the photometry over the field-of-view. The photometric calibration is based on nightly zeropoints, after which the overlaps between CCDs from the different dither positions are used to tie all CCDs and dither together, resulting in photometry consistent to the 1–2% level over the full field-of-view. Small absolute zeropoint offsets between pointings persist since the patchy distribution of the included survey tiles yet prevents a full cross-calibration. After solving for the astrometric solution of all dithers together, stacked images are produced together with weight maps, masks for bright stars and other image defects, and source catalogs. The stacked images provided in the public data releases form the input for our further analysis.

We carry out a point-spread function (PSF) homegenization across each image. This homogenization provides improved fixed aperture photometry, corrected shape measurements and, indirectly, refined colours and enhanced star-galaxy separation. The code for the PSF homogenization –described in (Pila-Díez et al. 2014)– measures the shapes of the bright stars across a given image, maps the varying PSF and finally convolves the map with a spatially variable kernel in order to return gaussian PSFs.

From these images, photometric "Gaussian Aperture and PSF (GAaP)" catalogues are produced using Gaussian aperture weight functions $\omega^2\cdot\exp[-r^2/2(\omega^2-p^2)]/(\omega^2-p^2)$ at the positions of SExtractor-detected sources. As long as the aperture radius ω is larger than the Gaussian PSF dispersion p, this aperture function yields the correct total flux for isolated point sources (irrespective of ω). For extended sources, however, these aperture fluxes increase with ω.

[1] http://kids.strw.leidenuniv.nl/DR2

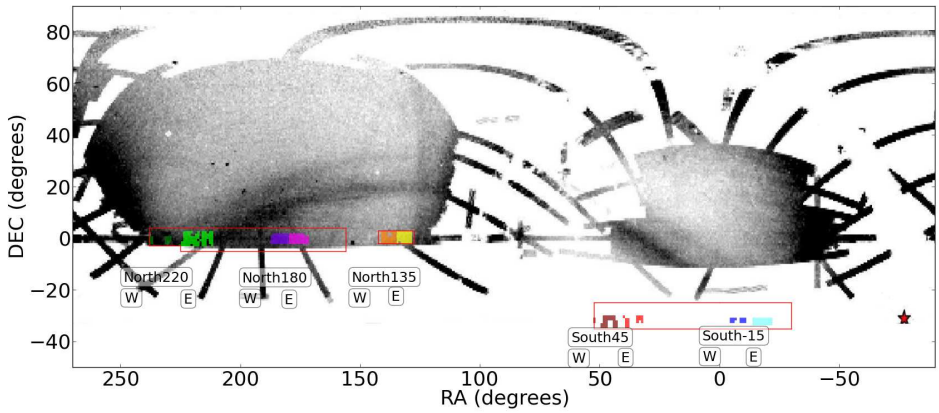

Figure 3.1: Equatorial map showing the position of all the KiDS fields used in this work (Data Releases 1 and 2). The different colours indicate the lines of sight in which the fields have been grouped to calculate the different density profiles. The background image is the SDSS-DR8 density map from Koposov et al. (2012), which shows the footprint of the Sagittarius stream and the location fo the Sagittarius dwarf galaxy. The red line denotes the expected KiDS footprint upon completion of the survey.

3.2.2 Catalogues

Stars and galaxies are separated by measuring their flux at $\omega = 0.5$" and 0.7" apertures in the r band, and keeping only those sources with $F_{0.5}/F_{0.7} \in [0.975, 1.025]$, that are detected at $> 5\sigma$ significance. A stellar completeness limit of $r = 23.2$ mag is imposed to avoid contamination by the small, round, fainter galaxies. And duplicate objects on overlapping tiles are removed.

The apparent magnitudes are dereddened using the interstellar extinction maps from Schlegel et al. (1998), and the GAaP photometry is corrected for a tile-based seeing dependency detected on the KiDS-to-SDSS offsets (see Figure 3.2). This dependency, a sign of residual flux at large radii after the PSF Gaussianization, is corrected through direct measurements (if the tile overlaps with SDSS data) or through a filter-specific interpolation. Once corrected for these offsets, GAaP provides a much smoother and flatter photometry on a star-by-star account than other photometry measuring tools, since it corrects for the PSF variation across each field of view. Last we transform the KiDS magnitudes to the SDSS system by appying the colour terms:

$$
\begin{aligned}
u_{SDSS} &= u_{KiDS} + 0.053 \cdot (u_{KiDS} - g_{KiDS}) - 0.0028 \cdot (g_{KiDS} - r_{KiDS}) \\
g_{SDSS} &= g_{KiDS} + 0.053 \cdot (g_{KiDS} - r_{KiDS}) \\
r_{SDSS} &= r_{KiDS} + 0.336 \cdot (g_{KiDS} - r_{KiDS}) \\
i_{SDSS} &= i_{KiDS} - 0.012 \cdot (r_{KiDS} - i_{KiDS}) - 0.0004 \cdot (g_{KiDS} - r_{KiDS})
\end{aligned}
$$

Table 3.1: Groups of pointings of KiDS as shown in Figures 3.1, 3.4, 3.5a and 3.6a. The table shows the central coordinates for each group, the number of individual fields of view contributing to it, its total area and the stellar completeness limit in the r band.

Group KiDS-	RA (deg)	Dec (deg)	l (deg)	b (deg)	$n_{\rm fields}$	Σ (deg^2)	$\rm mag_{lim,r,*}$
North220W	233.395758	0.12301	4.996485	42.63794	5	5.55	23.2
North220E	218.282384	-0.30425	348.794941	53.26131	24	24.45	23.2
North180W	183.806111	-0.02812	283.687780	61.48308	18	18.23	23.2
North180E	176.151782	-0.38023	269.928812	58.14329	19	18.29	23.2
North135W	138.175020	0.10505	230.730761	31.01870	17	18.49	23.2
North135E	131.554071	0.76375	226.214265	25.68091	20	19.78	23.2
South45W	46.602118	-32.24177	231.091424	-60.36720	8	9.68	23.2
South45E	35.744934	-31.99697	232.203287	-69.55028	6	5.52	23.2
South-15W	351.902387	-31.61901	14.081849	-71.22605	4	4.93	23.2
South-15E	342.302882	-31.81892	15.507201	-63.07876	12	13.29	23.2

The final photometry follows the expected colour-colour stellar loci from Covey et al. (2007) (see Figure 3.3).

Finally the KiDS fields are split in ten broad lines of sight based on their sky distribution (see Figure 3.1). The number of fields per line of sight, the central coordinates of these lines of sight and their affective area are recorded in Table 3.1. The effective areas have been calculated based on a finely spatially binned grid where we count the number of stars per bin as a way to determine the combined effect of masks and weights and tiles edges over the final catalogue of stars.

3.3 Stellar radial density profiles

3.3.1 Star selection and density profiles

We select near main sequence turnoff point (MSTO) stars as tracers for the overall stellar structure of the halo. To select them, we estimate their iron-to-hydrogen ratio and their absolute magnitude in the r band through two empirical photometric relations (Bond et al. (2010) and Ivezić et al. (2008), respectively):

$$[Fe/H] = -13.13 + 14.09x + 28.04y - 5.51xy - 5.90x^2 - 58.68y^2 + 9.14x^2y - 20.61xy^2 + 58.20y^3\,, \quad (3.1)$$

$$M_r = -0.56 + 14.32z - 12.97z^2 + 6.127z^3 - 1.267z^4 + 0.0967z^5 - 1.11[Fe/H] - 0.18[Fe/H]^2\,, \quad (3.2)$$

where $x = u - g$, $y = g - r$ and $z = g - i$. Relation 3.1 is valid in the $g - i < 0.6$ and $-2.5 \leq [Fe/H] \leq 0$ range, whereas relation 3.2 is valid in the $0.2 < g - i < 1.0$ range. Both regimes are compatible (and –for a small range– smoothly extrapolatable) to the colour regime of the nearMSTO stars.

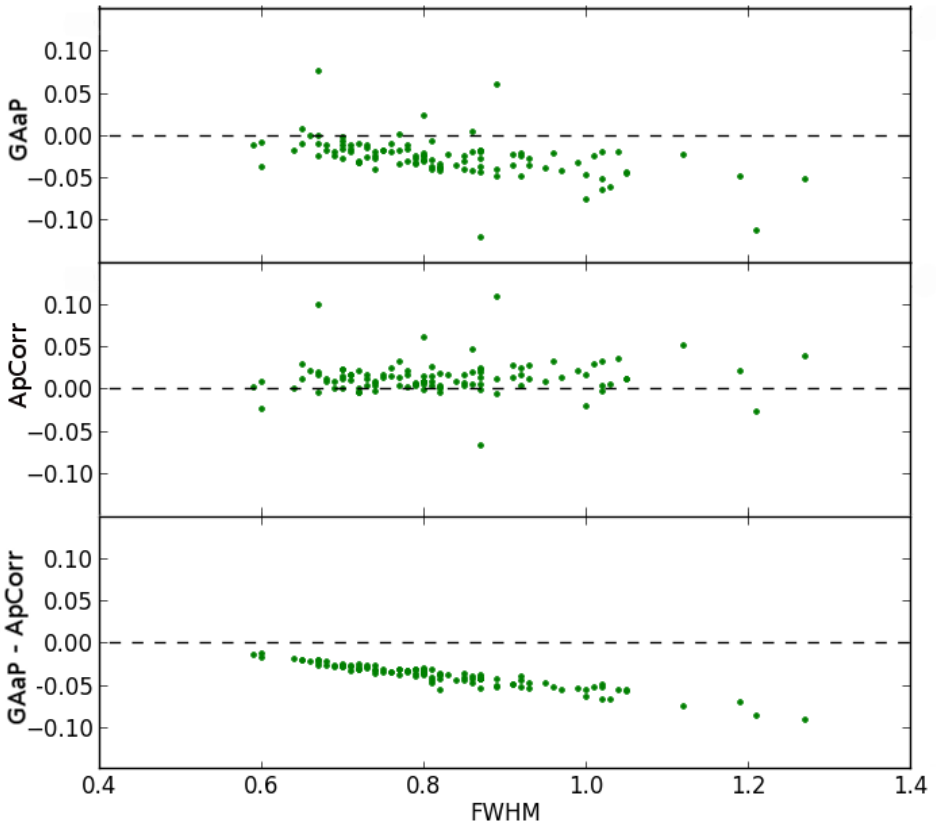

Figure 3.2: Relation between the KiDS-to-SDSS photometric offsets and the full-width at half-maximum (FWHM) in the g band for all the KiDS tiles that overlap with SDSS data. **Top:** KiDS-to-SDSS offsets based on GAaP photometry. The average offsets depart from zero with incresing FWHM. **Centre:** KiDS-to-SDSS offsets based on aperture-corrected photometry. The average offsets stay close to zero for all values of FWHM. **Bottom:** difference between the top and central panels (between GAaP and aperture-corrected photometries), to remove the tile-based scatter and illustrate the seeing dependency in GAaP. A similar relation is observed for the u, r and i filters.

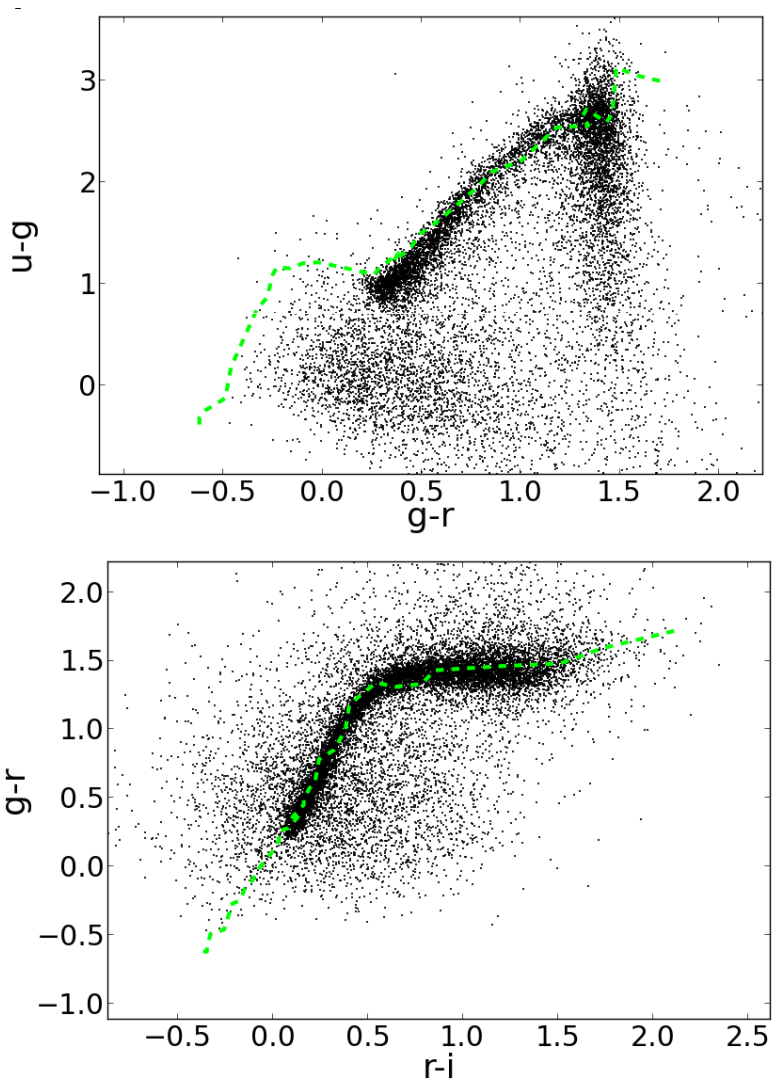

Figure 3.3: Colour-colour diagrams (CCDs) corresponding to one of the tiles in KiDS-North135E. The sources in the stellar catalogue (black) have been calibrated to SDSS's stellar photometry. The main sequence stellar loci (green dashed lines) are from Covey et al. (2007) (Tables 3 and 4).

We use the following cuts on the stellar colours, estimated [Fe/H] and estimated M_r to isolate the halo nearMSTO stars:

$$0.2 < g - r < 0.3\,; \tag{3.3}$$
$$g, r, i > 17\,; \tag{3.4}$$
$$0.1 < g - i < 0.6\,; \tag{3.5}$$
$$5.0 > M_r > -2\,; \tag{3.6}$$
$$-2.5 \leq [Fe/H] \leq 0\,. \tag{3.7}$$

These cuts provide a subset of halo, metal poor, distant, main sequence F stars and help decrease the contamination by quasars and white-dwarf/M-dwarf pairs (see Covey et al. (2007) for a general reference, or Pila-Díez et al. (2015) for an application to nearMSTO halo stars).

We derive the distance modulus and the heliocentric distance for each nearMSTO star from the estimated absolute brightness. At the stellar completeness limit of KiDS, this allows us to reach as far out as 60 kpc. We bin the nearMSTO stellar distribution in units of size $\Delta\mu = 0.2$ mag. We count the stars in each bin and calculate the stellar number density and its uncertainty (through partial derivatives) for the different lines of sight:

$$\rho_{l,b,D} = \frac{N_{l,b,\Delta\mu}}{0.2 \cdot ln(10) \cdot D_{hC}^3 \cdot \Delta\Omega \cdot \Delta\mu}\,; \tag{3.8}$$
$$E_\rho = \sqrt{(\frac{\rho}{\sqrt{N}})^2 + (\frac{\rho}{\sqrt{n_{fields}}})^2}\,. \tag{3.9}$$

where $N_{l,b,\Delta\mu}$ is the number of stars per bin in a given direction of the sky, D_{hC} is the heliocentric distance, $\Delta\Omega$ is the spherical area of each line of sight, and l and b denote the galactic coordinates for that line of sight. In practical terms:

$$\Delta\Omega = \frac{4\pi}{41253}\Sigma(\mathrm{deg}^2)\,, \tag{3.10}$$

where (Σ) is the effective area of each line of sight (Table 3.1).

The resulting density profiles are illustrated in Figure 3.4 for galactocentric distances. The figures and the following analysis and discussion are restricted to bins that meet $R_{GC} > 5$kpc, $|z| > 10$ kpc and a distance modulus of $\mu \leq mag_{lim} - 4.5 = 18.7$ mag (to avoid the Galactic thick disk and for completeness[2] of the faintest near-MSTO stars, respectively).

3.3.2 Fitting procedure

We fit a number of structural models of the Galactic stellar halo to the density profiles, first by only fitting the KiDS lines of sight, and later by fitting both the

[2]The incompleteness in the $mag_{lim} - 5.0 \leq \mu \leq mag_{lim} - 4.5$ distance range originating in equation 3.6 is on average 20% of the total number of near-MSTO stars present within the same distance range.

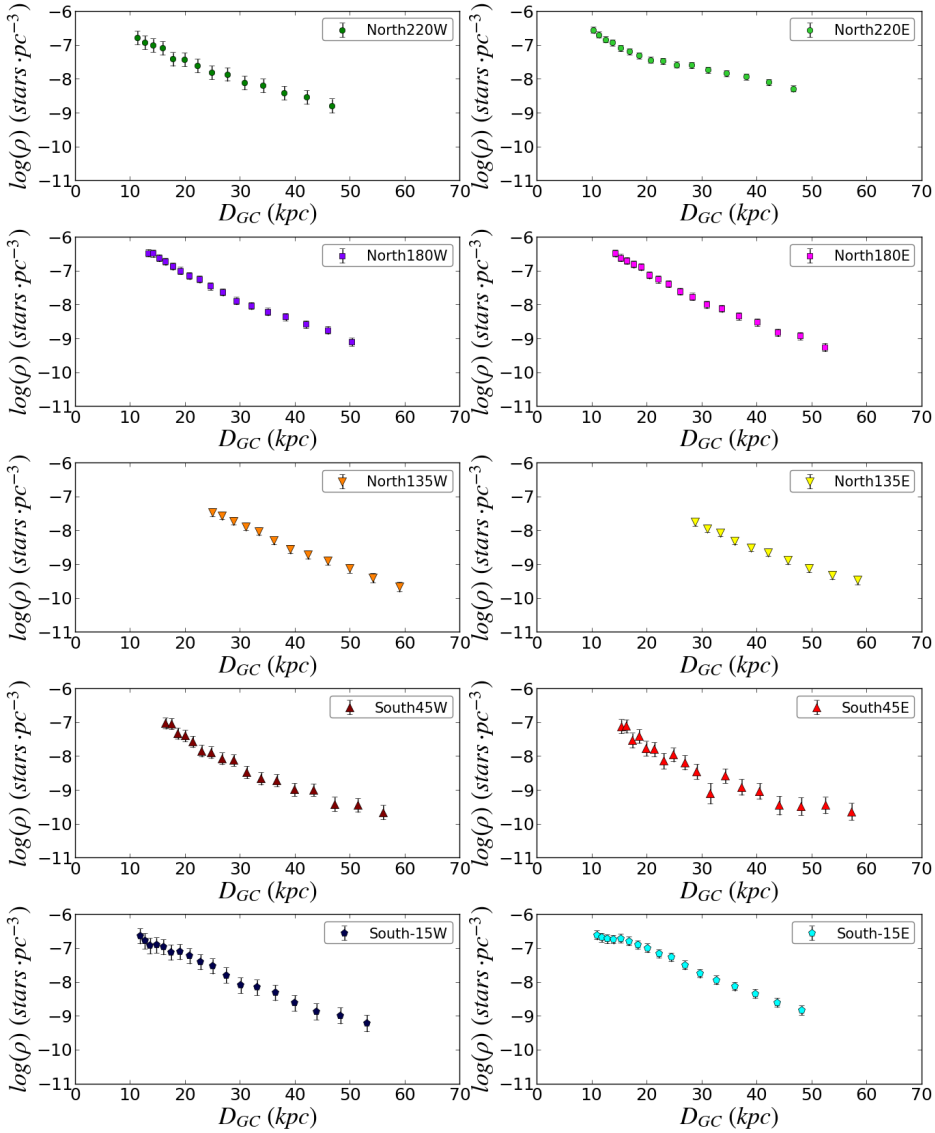

Figure 3.4: Stellar density profiles versus galactocentric distance for the near Main Sequence turnoff point stars (nearMSTO) from the KiDS lines of sight KiDS-North220W (dark green), KiDS-North220E (light green), KiDS-North180W (purple), KiDS-North180E (pink), KiDS-North135W (orange), KiDS-North135E (yellow), KiDS-South45W (brown), KiDS-South45E (red), KiDS-South-15W (blue) and KiDS-South-15E (cyan). Their colours match those in Figure 3.1.

KiDS and the CFHT-INT lines of sight presented in Pila-Díez et al. (2015) since the combination provides a more complete view of the stellar halo and returns better constraints.

The models are expressed in the galactocentric cartesian coordinate system (x, y and z). For the heliocentric to the galactocentric transformation, we assume that the Sun is located at (8,0,0) kpc (Malkin 2012). We fit the following models:

- Axisymmetric model:

$$\rho(x,y,z) \quad = \quad \rho_0 \cdot \left(x^2 + y^2 + \frac{z^2}{q^2} \right)^{n/2}, \tag{3.11}$$

  where $q = c/a$ is the polar axis ratio (or oblateness) of the halo.

- Triaxial model:

$$\rho(x,y,z) \quad = \quad \rho_0 \cdot \left(x^2 + \frac{y^2}{w^2} + \frac{z^2}{q^2} \right)^{n/2}, \tag{3.12}$$

  where $w = b/a$ is the axis ratio in the Galactic plane.

- Broken power law (change in the power index at R_{break}):

$$\rho(x,y,z) = \begin{cases} \rho_0 \cdot (R_{ellip})^{\,n_{in}}, & R_{ellip} < R_{break} \\ \rho_0 \cdot (R_{ellip})^{\,n_{out}} \cdot R_{break}^{\,n_{in}-n_{out}}, & R_{ellip} \geq R_{break} \end{cases} \tag{3.13}$$

$$R_{ellip} = \left(x^2 + y^2 + \frac{z^2}{q^2} \right)^{1/2}$$

- Double broken power law (change in the power index and the oblateness at R_{break}):

$$\rho(x,y,z) = \begin{cases} \rho_{0,in} \cdot \left(x^2 + y^2 + \frac{z^2}{q_{in}^2} \right)^{n_{in}/2}, & R_{GC} \leq R_{break} \\ \rho_{0,out} \cdot \left(x^2 + y^2 + \frac{z^2}{q_{out}^2} \right)^{n_{out}/2}, & R_{GC} > R_{break}\,. \end{cases} \tag{3.14}$$

We fit all these models to the data using Python's "curve-fit" method from its Scipy.optimize library (built on the Levenberg-Marquardt algorithm) in order to obtain the best fit values for the structural parameters. For the double broken power law model, we use a fixed value of R_{break}, which is the one suggested by the best fit of the simple broken power law model. Additionally, for the triaxial and the simple broken power law models, we also explore the fits to the data through a grid of fixed parameters where only the density scale factor (ρ_0) is allowed to vary freely. This allows us to evaluate the structural parameters in those cases where

the model is overparameterized in relation to the available data, and to check for local minima. The grids are built so that the different parameters evolve in the following ranges with specific incremental steps (δ): $q^2, w^2 \in [0.1, 2.0; \delta = 0.05]$, $n \in [-5.0 - 1.0; \delta = 0.1]$, $n_{in} \in [-4.0, -1.0; \delta = 0.1]$, $n_{out} \in [-7.0, -3.0; \delta = 0.2]$.

We determine the best-fit parameters by minimizing

$$\chi^2 = \sum_{i=1}^{N_{data}} \left(\frac{\rho_{data,i} - \rho_{model,i}}{E_{\rho,i}} \right)^2 . \tag{3.15}$$

We use its corresponding reduced expression for analysis and comparison between the models:

$$\chi^2_{red} = \frac{\chi^2}{N_{data} - N_{params}} , \tag{3.16}$$

whith N_{data} and N_{params} being the number of data bins and the number of free parameters in the model, respectively.

We mask out certain distance bins in the different lines of sight so that they are not considered for the models fitting. These masked regions correspond to the (3D) location of known halo stellar overdensities. In particular we excise the Sagittarius stream in the KiDS-North220 and KiDS-South-15 fields (at $D_{helioC} \in [30, 60]$ kpc and $D_{helioC} \in [15, 35]$ kpc, respectively), the Virgo Overdensity in the KiDS-North180 fields (at $D_{helioC} \in [6, 25]$ kcp) and the antincentre substructures –the Monoceros ring, the Eastern Band Structure (EBS) and the Anti Centre Structure (ACS)– in the KiDS-North135 fields (at $D_{helioC} \in [9, 15]$ kpc). As noted in Pila-Díez et al. (2015), not removing the substructure can have an impact on the structural parameters, with variations of $0.2 - 0.4$ for the inner power law index and 15% on the disk axis ratio, but not necessarily limited to these values or these parameters.

Finally we test the influence of the photometric uncertainties on the best fit values through a set of Monte Carlo simulations. We randomly modify the u, g, r, i magnitudes of each star within the boundaries provided by their photometric uncertainties, and produce a large number of mock catalogues. By fitting the axisymmetric model to each of them, we can create a statistic on the resulting structural parameters. We find that their variation is well accounted for by the statistical uncertainties returned by the fits, meaning that the simulated parameters fall within 1σ of our observed parameters.

3.3.3 Results

The best fit parameters for the independent fit of the ten KiDS lines of sight, for the independent fit of the eight CFHT-INT lines of sight (Pila-Díez et al. 2015) and for the combined fit of the KiDS plus the CFHT-INT lines of sights are presented in Tables 3.2, 3.3 and 3.4. The best fit parameters resulting from the grid fits are signaled by an asterisk after the name of the model and after the χ^2_{red} value. In the case of the triaxial model for the combined surveys, two

values of χ^2_{red} (resulting from the free-parameters fitting and the gridded fitting) are quoted, with both having converging best fit values for the paremeters.

The density profiles and the best fit models for the combined lines of sight are illustrated in Figure 3.5, where the masked out regions containing known substructure have been indicated with grey areas. The data-to-model residuals for the best fits of the combined lines of sight are shown in Figure 3.6.

If we compare the χ^2_{red} in Tables 3.2, 3.3 and 3.4, two facts become apparent. The first one is that the χ^2_{red} of the CFHT-INT-only fits are systematically smaller than those of the KiDS-only and KiDS plus CFHT-INT fits. This suggests that the KiDS density profiles deviate more strongly from a smooth halo, be it because of accreted overdensities or because of actual departures of the smooth halo from the models. Considering that the KiDS-North135W/E and the KiDS-South45W/E profiles follow the models perfectly (see Figure 3.6a), we rule out an intrinsic bias in the KiDS photometric calibration as the possible cause of the χ^2_{red} differences.

The second fact is that, in the three first fitting scenarios (axisymmetric, triaxial and simple broken power law model), the χ^2_{red} tends to decrease with model complexity. In particular, the χ^2_{red} suggests that the simple broken power law performs better than the triaxial and axisymmetric models, even if we account for the difference in the number of parameters between a free fit and a grid fit. The triaxial model performs slightly better than the axisymmetric model in the KiDS-only fits, but returns an extreme best fit value for the disk axis ratio ($w = 1.4 \pm 0.1$) and shows a large degeneracy along w. This suggests that the geometry of the KiDS footprint is not enough to constrain a possible triaxiality. When analysed for the CFHT-INT-only or the combined fits, the triaxiality loses any degeneracy and comes in agreement with inner Galaxy measurements ($w = 0.87 \pm 0.09$ and $w = 0.94 \pm 0.05$, respectively); however, it does this at the expense of a χ^2_{red} equal (once we take into account the smaller number of free parameters in the grid fits) to that of the axisymmetric model and converging ρ_0, n and q parameters. This is suggestive of a very mild triaxiality.

In general, all the fits –except that of the degenerate triaxial model fit to KiDS-only data– agree on a global power law index within $n \in [-4.2, -4.4]$, an outer power law index within $n_{out} \in [-4.6, -5.0]$ (including uncertainties) and a polar axis ratio within $q \in [0.74 \pm 0.05, 0.81 \pm 0.05]$. However, the different sets of fitted data return different break distances, R_{break}, that also affect the values of the inner power law index, n_{in} (from 19.0 ± 0.5 kpc to 30.5 ± 0.5 kpc and -2.45 ± 0.05 to -3.70 ± 0.05, respectively). We will discuss this further in section 3.4.2.

Finally, it is worth noting that both in the KiDS-only fits and the KiDS plus CFHT-INT fits, the complex broken power law model (the one with two possible values for n and for q) returns best fit values for the inner and outer oblatenesses that are in agreement with each other and with the oblateness of the other models (within uncertainties). This suggests that, based on our data, there is no need for a break in the polar axis ratio.

Table 3.2: Best fit parameters for the four different Galactic stellar distribution models fitted to the ten KiDS lines of sight. The data that is affected by known halo substructures (the Sagittarius stream, the Virgo Overdensity and the anticentre substructures) have been masked out for the fitting. Models and χ^2_{red} signaled with an asterisk indicate that their best fit values are the result of fitting through a parameter grid, and therefore have intrinsically smaller χ^2_{red} than those resulting from an all-free-parameters fit.

Model	χ^2_{red}	$\rho_0\,(\mathrm{pc}^{-3})\cdot 10^{-3}$	R_{break} (kpc)	n	n_{in}	n_{out}	q	q_{in}	q_{out}	w
axisymmetric	2.30	23 ± 8	–	-4.31 ± 0.08	–	–	0.79 ± 0.04	–	–	–
triaxial*	2.15*	13 ± 1	–	-4.30 ± 0.05	–	–	0.89 ± 0.05	–	–	1.4 ± 0.1
broken p.l.$_n$*	2.09*	3.9 ± 0.2	30.5 ± 0.5	–	-3.70 ± 0.05	-5.00 ± 0.05	0.81 ± 0.05	–	–	–
broken p.l.$_{n,\,q}$	1.39,2.86	5.3 ± 6	30.5_{fixed}	–	-3.8 ± 0.3	-4.9 ± 0.3	–	0.8 ± 0.1	0.79 ± 0.06	–
initial parameters	–	0.001	40.0	-3.00	-3.00	-3.50	0.70	0.70	0.8	1.00

Table 3.3: Same as in Table 3.2 but this time fitting the models to the CFHT-INT data (as presented in Table 2 of Pila-Díez et al. (2015)).

Model	χ^2_{red}	$\rho_0\,(\mathrm{pc}^{-3})\cdot 10^{-3}$	R_{break} (kpc)	n	n_{in}	n_{out}	q	q_{in}	q_{out}	w
axisymmetric	1.90	14 ± 6	–	-4.31 ± 0.09	–	–	0.79 ± 0.06	–	–	–
triaxial*	1.86*	14 ± 6	–	-4.28 ± 0.09	–	–	0.77 ± 0.06	–	–	0.87 ± 0.09
broken p.l.$_n$*	1.52*	0.071 ± 0.003	19.0 ± 0.5	–	-2.40 ± 0.05	-4.80 ± 0.05	0.77 ± 0.03	–	–	–
broken p.l.$_{n,\,q}$	1.99,1.51	1 ± 3	19_{fixed}	–	-3.3 ± 0.6	-4.9 ± 0.2	–	0.7 ± 0.2	0.88 ± 0.07	–
initial parameters	–	0.001	40.0	-3.00	-3.00	-3.50	0.70	0.70	0.8	1.00

Table 3.4: Same as in Table 3.2 and Table 3.3 but this time fitting the models to both the KiDS and the CFHT-INT data.

Model	χ^2_{red}	$\rho_0\,(\mathrm{pc}^{-3})\cdot 10^{-3}$	R_{break} (kpc)	n	n_{in}	n_{out}	q	q_{in}	q_{out}	w
axisymmetric	2.53	16 ± 5	–	-4.27 ± 0.07	–	–	0.75 ± 0.03	–	–	–
triaxial	2.53//2.50*	17 ± 5	–	-4.26 ± 0.07	–	–	0.74 ± 0.04	–	–	0.94 ± 0.05
broken p.l.$_n$*	2.36*	0.10 ± 0.01	19.0 ± 0.5	–	-2.45 ± 0.05	-4.6 ± 0.05	0.74 ± 0.05	–	–	–
broken p.l.$_{n,\,q}$	1.80,2.64	1 ± 2	19.0_{fixed}	–	-3.3 ± 0.5	-4.6 ± 0.1	–	0.8 ± 0.1	0.76 ± 0.04	–
initial parameters	–	0.001	40.0	-3.00	-3.00	-3.50	0.70	0.70	0.8	1.00

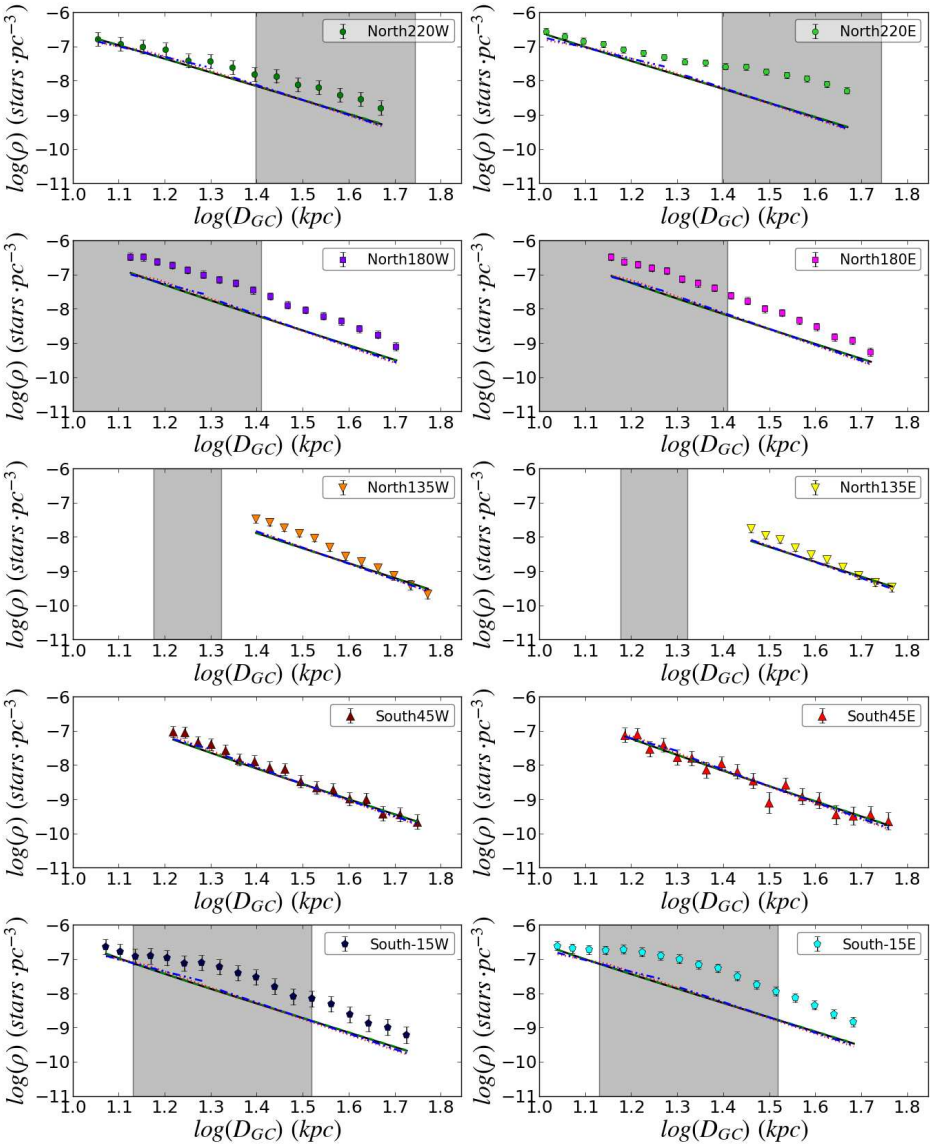

(a) Fitted density profiles for the KiDS lines of sight.

Figure 3.5: Density profiles in decimal logarithmic scale and the models' best fits from Table 3.4 for the KiDS lines of sight. The different lines represent the axisymmetric (black solid line), the triaxial (green dashed line), the broken power law with varying power index (red dotted line) and the broken power law with varying power index and oblateness (blue dashed-dotted- dotted line) models. The grey areas denote data that have been masked from the fitting due to the presence of substructure.

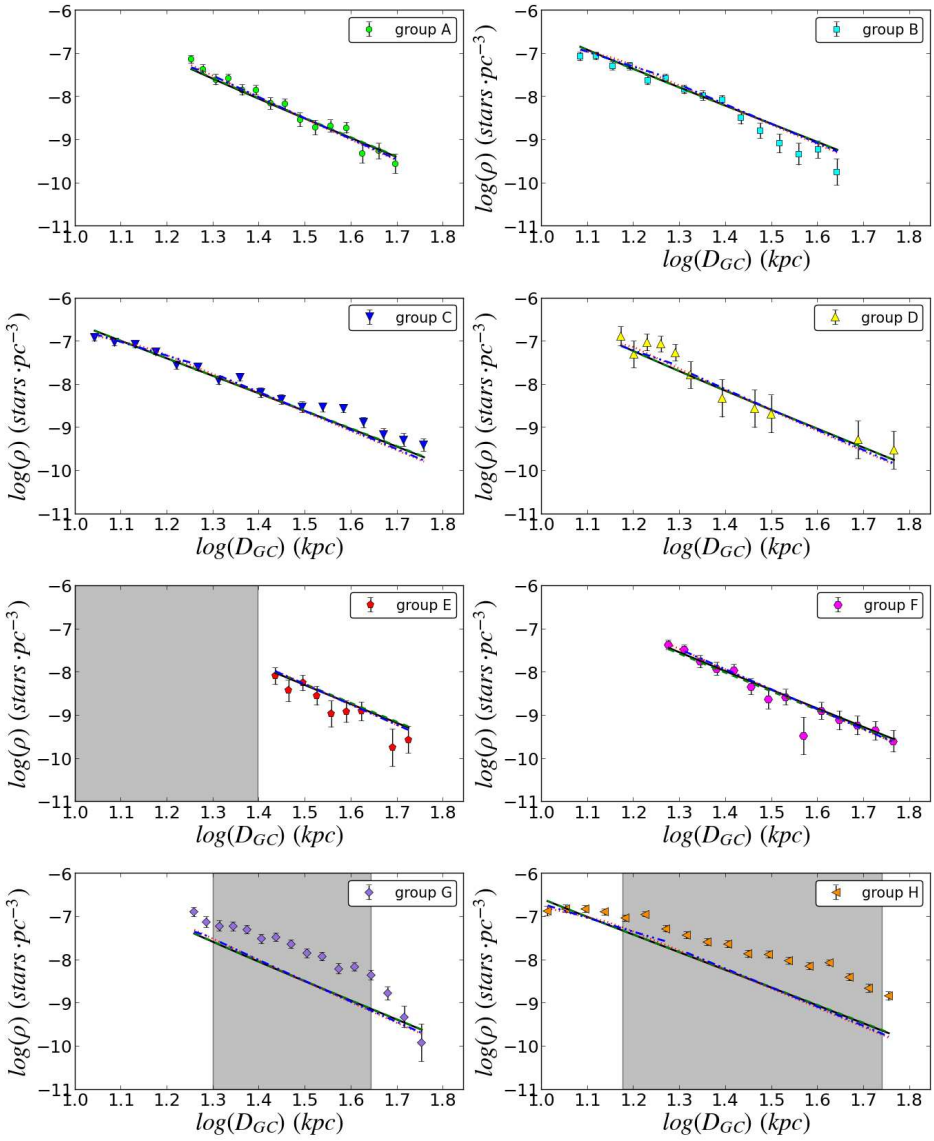

(b) Fitted density profiles for the CFHT-INT lines of sight.

Figure 3.5: Density profiles in decimal logarithmic scale and the models' best fits from Table 3.4 for the CFHT-INT lines of sight. The different lines and the shaded areas follow the same code as in Figure 3.5a.

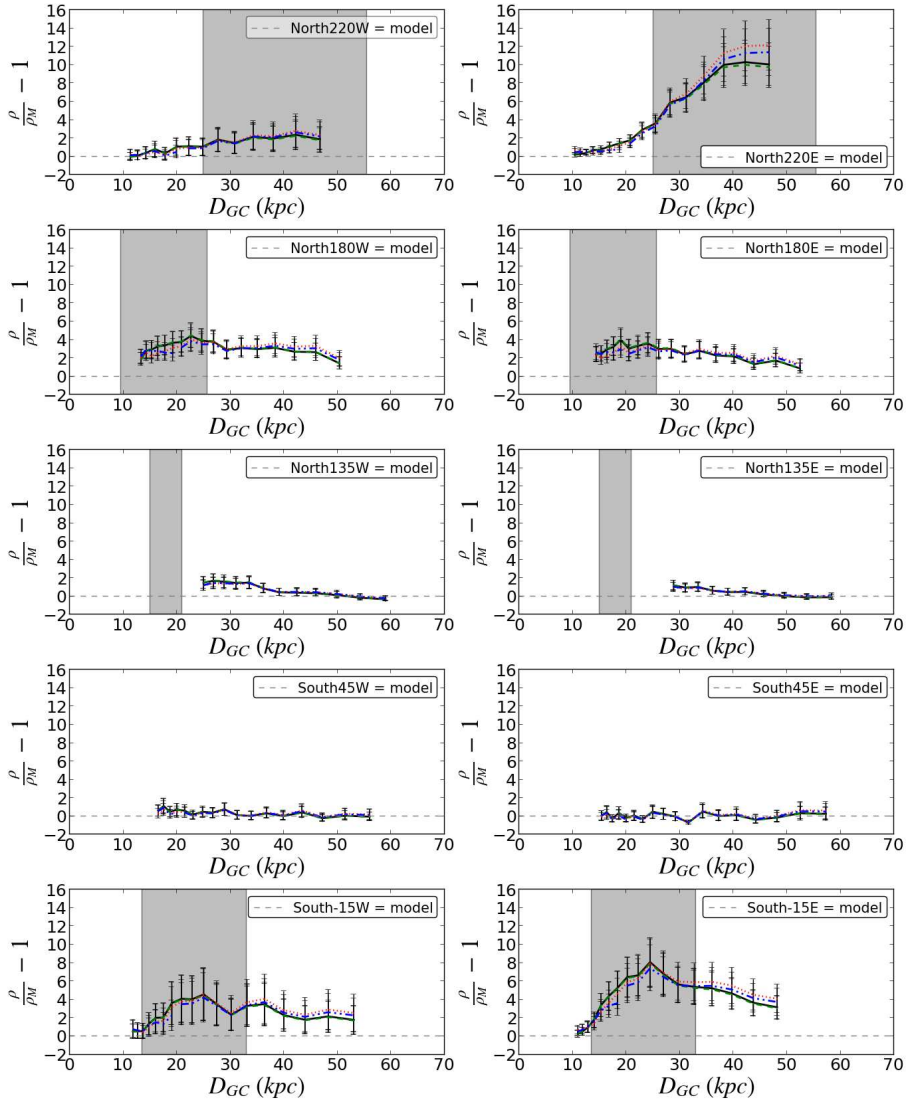

(a) Data-to-model residuals for the KiDS lines of sight.

Figure 3.6: Residuals between the data and the models' best fits from Table 3.4 for the KiDS lines of sight. The different lines and the shaded areas follow the same code as in Figure 3.5a.

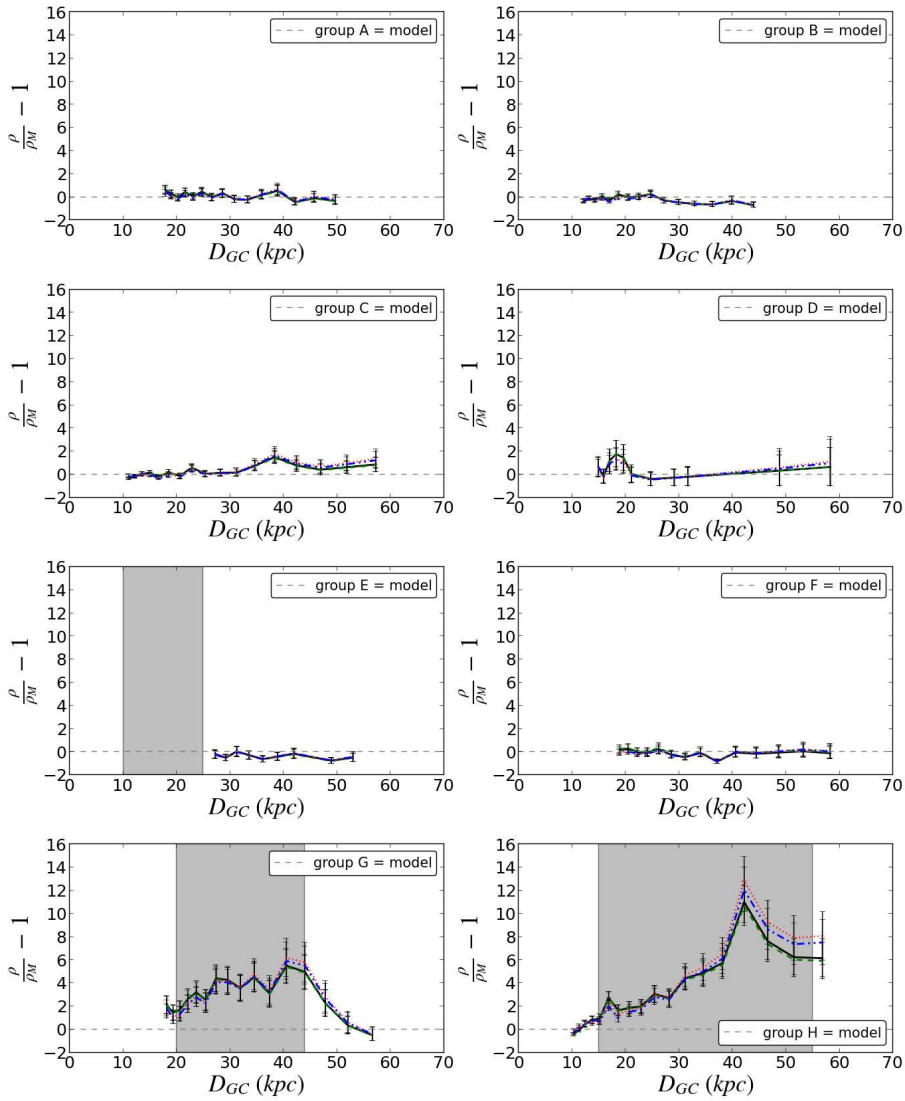

(b) Data-to-model residuals for the CFHT-INT lines of sight.

Figure 3.6: Residuals between the data and the models' best fits from Table 3.4 for the CFHT-INT lines of sight. The different lines and the shaded areas follow the same code as in Figure 3.5a.

3.4 Discussion

3.4.1 Robustness of the best fit structural parameters

We test the influence of the different lines of sight on the best fit parameters in search for potential sources of bias. For this, we remove the KiDS lines of sight one at a time and perform the free-parameters fits for the axisymmetric, triaxial and simple broken power law models on the KiDS plus CFHT-INT density profiles (a similar test for CFHT-INT-only lines of sight can be found in Pila-Díez et al. (2015)).

By doing this for the axisymmetric model, we find that any line of sight removal keeps the n new values within the uncertainties of the overall results. However removing KiDS-North180W/E from the set decreases q slightly beyond the uncertainty of the overall oblateness, while removing KiDS-North135W/E increases it in a similary manner. Those same lines of sight move the n values in the same directions, but within the uncertainty limits.

Checking for the triaxial model, we find that in this case any line of sight removal keeps the n, q and w new values within the uncertainties of the overall results, with no significant deviations. KiDS-North180W/E and KiDS-North135W/E seem to have the largest influences in the same directions they had for the axisymmetric case. Additionally, removing one of KiDS-North135W/E decreases w the most.

Finally we test the influence of the different lines of sight for the freely fit simple broken power law model. When fitting all the available lines of sight, the returned parameters were unconstrained and the break distance was much larger than the distances probed by our data. This motivated the use of a parameters-grid for fitting. When we remove the KiDS lines of sight one at a time, we find a similar behaviour in all the cases except that of KiDS-North180W. Interestingly, removing this line of sight returns constrained values for the parameters, meaning that this is the line of sight introducing most of the uncertainty into the fit(s). In practice, however, we cannot exploit this improvement in the fits to our advantage, because removing KiDS-North180W places the break distance beyond the scope of our data, at $R_{break} = 65 \pm 7$ kpc, with a $\chi^2_{red} = 2.28$, effectively representing an axisymmetric model.

Overall, we can conclude that removing any single line of sight does not significantly change the fit results.

3.4.2 KiDS vs CFHT-INT

When fitting the axisymmetric model to either one of the two surveys or to their combination, although the χ^2_{red} for the KiDS fit worsens (it is 20% larger than for the CFHT-INT fit), the three fits return consistent results for the halo structural parameters.

When fitting for triaxiality, it is clear that the w value found for the KiDS fit is large and implausible, as compared to previous measurements of the disk axis

ratio and our current knowledge of the Milky Way. The reason for this improbable value is that there is only one line of sight in our KiDS data set at reasonably low Galactic latitude, and therefore the constraining power for w is poor. Once combined with the CFHT-INT data set, the constraining power increases and returns values within the anticipated range. As it should be expected for a value of w close to 1, all the triaxial model fits return values for the other parameters in agreement with those of the axisymmetric model fits.

For the broken power law model, the fits to the different data sets return comparable results for the outer halo (n_{out}) and the oblateness. This can be explained by the fact that both surveys amply sample the outer halo, with most data points at distances larger than 25 kpc. The only real inconsistency between the fits to the two data sets happens for the break radius and, subsequently, for the inner power law index (n_{in}), which we investigate further.

The colour maps and isocontours in Figure 3.7 map the best fits χ^2_{red} values for different values of the structural parameters for the KiDS (left), the CFHT-INT (centre) and the combined data sets (right). It becomes clear from these diagrams that the break distance is poorly constrained, and that n_{in} is strongly dependent on the survey. In the case of the KiDS-only fits, the best fit values of n_{in} are a function of the best fit values of R_{break}. In the case of CFHT-INT-only and the combined surveys, the fits favour a small value for R_{break}, but at the same time the sparsity of data points at $R_{GC} < 20$ kpc renders the value of n_{in} degenerate.

An explanation for this degeneracy of n_{in} and for such a small absolute best fit value of R_{break} in the CFHT-INT and the combined data sets lies within the density profiles. A close inspection of the density profiles shows that these break distance values match the distance where most of the CFHT-INT lines of sight are beginning. Particularly, only three out of the eight lines of sight are contributing density bins below the 19 kpc threshold (lines B, C and H), and only two of those three are fitted uninterruptedly further out, probing the alleged transition (H is masked out at $D_{helioC} = 20$ kpc or $R_{GC} = 15$ kpc). This suggests that the fitting algorithm is indeed trying to adjust to the lack of data rather than trying to fit a true transition within the data. The disappearance of the n_{in} degeneracy beyond $R_{break} > 22$ kpc suggests that the true value of the break distance lies somewhere between this transition point and the value suggested by the KiDS-only lines of sight. This is, somewhere between 22 kpc and 31 kpc, rather than at 19 kpc. An exploration of the grid parameters and their χ^2_{red} when the break distance is fixed at the average value from the literature (27 kpc, see Table 3.5), shows that the best fit in such a case holds a practically identical value of χ^2_{red} to that of the absolute minimum (with a difference of only 1.7%).

In conclusion, the relatively small amount of data at $R_{GC} < 30$ kpc causes us to be unable to constrain R_{break} very well, and probably introduces a bias towards small R_{break} values and degenerate n_{in} values through the CFHT-INT data set. Ideally, with more data available at short galactocentric distances in a wider survey (or combination of surveys), one would fit models of both the thick disk and the halo, as a way to remove our $|z| > 10$ kpc constraint on the density

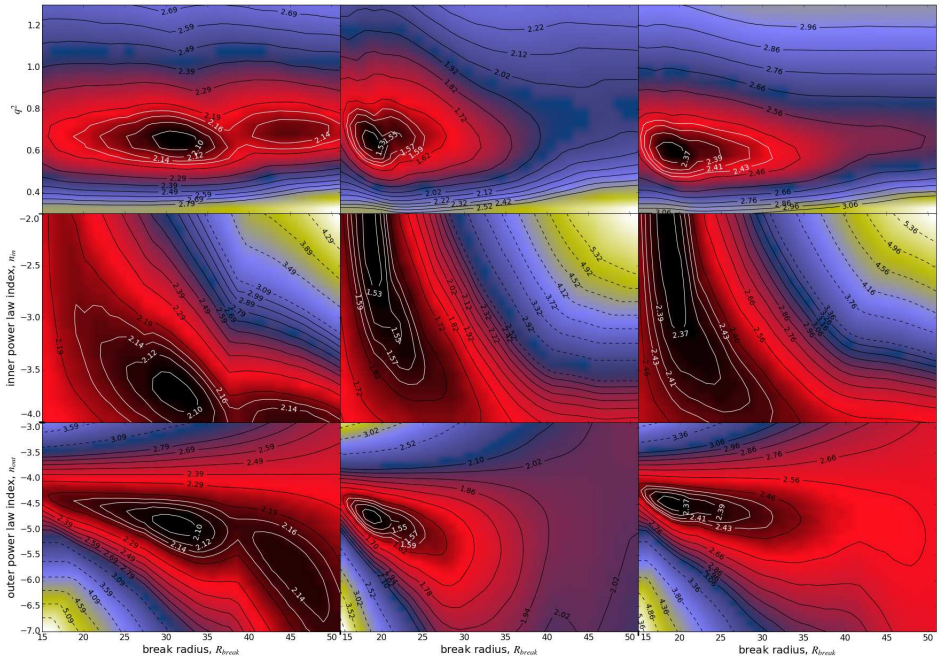

Figure 3.7: χ^2_{red} isocontours maps showing the relation between a given structural parameter and the break distance based on the grid fits for the simple broken power law model. **Left panels:** fits to the KiDS data set. **Central column panels:** fits to the CFHT-INT data set. **Right panels:** fits to the combined data sets. **Top panels:** polar axis ratio versus break distance. **Central row panels:** inner power law index versus break distance. **Bottom panels:** outer power law index versus break distance.

profile bins that are used for fitting. This procedure would allow to fit the halo at smaller radii, while also preserving the excellent handle on the outer reaches afforded by the KiDS and CFHT-INT deep photometry. Of course, this approach comes at the cost of increasing the complexity by forcing to consider both the halo and the thick disk. This has been done by Robin et al. (2014), who used their SDSS plus 2MASS data to explore the thick disk and the halo mostly out to $R_{GC} < 30$ kpc. Their fits favour a break distance located at $R_{break} > 30$ kpc, but it would seem plausible that their lack of data at larger distances prevents them from detecting a closer break distance, just like our lack of data at short distances prevents us from constraining it.

3.4.3 Comparison to previous studies

We compare our results on the structural parameters of the stellar halo to several previous results in the literature, namely: Jurić et al. (2008), Sesar et al. (2011),

Deason et al. (2011), Robin et al. (2014), de Jong et al. (2010), Chen et al. (2001), Bell et al. (2008), Faccioli et al. (2014), Sesar et al. (2010a), Watkins et al. (2009) and Pila-Díez et al. (2015). The results, stellar tracers and distance ranges of these works have been summarized in Table 3.5. A detailed description of their geometry and sky coverage can be found in Pila-Díez et al. (2015).

Although RRLyrae stars have been used as stellar halo tracers out to 110kpc, our data allows us to construct stellar density profiles further out (up to 60 kpc) than any previous analysis. This provides us with an unprecedented constraining power for the outer stellar halo, only comparable to the results presented in Pila-Díez et al. (2015).

In our previous work we already noted that all surveys that reach beyond $R_{GC} = 30$ kpc seem to agree on the need for a break in the power law index. The difference between n, n_{in} and n_{out} for the different surveys is probably not only an effect of the different geometries of the surveys but also a reflection of their different distance ranges and of the sharp or progressive steepening of the halo. The fact that the different works fail to find a consensual break distance or consensual power index values, together with the degeneracy that we detect between n_{in} and R_{break}, are in support of this interpretation.

Nonetheless and independently of the exact interpretation, these works find the break distance to be located between 20 and 34 kpc. The best fit values for R_{break} for the CFHT-INT and the KiDS individual data sets (19.0 ± 0.5 and 30.5 ± 0.5, respectively) lie near the opposite extremes of this distance range, but, as discussed in section 3.4.2, the degeneracy between n_{in} and R_{break} suggests more reliable values in the $[22, 30)$ kpc range.

Several of the other studies that are limited to Galactocentric distances smaller than 30 kpc and only fit a single power law index to the halo, provide indices in the $[-3.3, -2.5]$ range. The n_{in} values of the studies that do detect a break in the power law are roughly consistent with this range, with the most significant discrepancy coming from our KiDS-only result and our KiDS plus CFHT-INT result in case of a large value for R_{break}. For the outer halo, power law indices are generally found to be in the $[-3.5, -5.8]$ range, although the majority of studies seems to cluster around -4.0. Again, the values for n_{out} that we find for our data sets are on the steeper side of the distribution (between -4.6 and -5.0). The recovered steepness of the power law might be related to the inclusion or removal of large, known substructures in the fitted data, as also noted by Robin et al. (2014). In Pila-Díez et al. (2015) we showed that in the case of our CFHT-INT data set the inclusion of the Sagittarius stream leads to a power-law index that is 0.2 dex smaller for the axisymmetric and triaxial halo models. Keeping in mind this effect, together with the fact that our data probes the underlying stellar density distribution of the outer halo further out than other data sets, we conclude that the smooth outer halo follows a power law with index close to -4.6.

The oblateness values of several previous works seem to agree in $0.55 \leq q \leq 0.70$, with the only clear exception of de Jong et al. (2010) ($q = 0.88 \pm 0.03$) and the wider Bell et al. (2008) ($q \in [0.5, 0.8]$). Our results, both for the KiDS-only,

for the CFHT-INT-only and for the combined triaxial and broken fits, all fall in the higher-end of this range, with values within 0.74 ± 0.05 and 0.81 ± 0.05. Therefore it seems safe to conclude that the stellar halo is moderately oblate, and is best represented by a steepening of the density profile at distances larger than 25 kpc.

We also find that a very mild triaxiality ($w = 0.94 \pm 0.05$) is a good representation of the stellar halo, although we do not test this hypothesis in combination with the broken power law model for the sake of simplicity and proper parametrization. The only other works that reported specific values on the triaxiality are Bell et al. (2008) and our previous study with CFHT-INT-only data. Both found that $w \geq 0.8$.

3.4.4 Detection of overdensities and identification

Finally, we look for overdensities in the data-to-model residuals (Figure 3.6) of the KiDS lines of sight, since the CFHT-INT lines of sight were already discussed in Pila-Díez et al. (2015).

We find that the density profiles for regions KiDS-North135W, KiDS-North135E, KiDS-South45W and KiDS-South45E follow the models quite well, with a brief maximum deviation of a factor of 2 for KiDS-North135W.

We also find a very clear overdensity matching the expected distances for the Sagittarius (Sgr) stream in the KiDS-North220E line of sight. We note that this overdensity already starts to smoothly build up as early as $R_{GC} = 20$ kpc, and reaches its maximum (a factor of ~ 10) at around 40 kpc. KiDS-North220W, on the contrary, displays a very mild and constant overdensity of only a factor of 2^{+2}_{-1}. This could indicate that the KiDS-North220W is only partially probing the Sgr stream, that it is probing a less dense region of the stream or that there is no contribution from a stream but simply a departure of the smooth halo component from the theoretical model.

The lines of sight corresponding to the KiDS-North180W and KiDS-North180E regions depart from the models at all probed distances. In the $R_{GC} \in [10, 27]$ kpc range, we were expecting an overdensity caused by the Virgo overdensity. However, the residuals barely decrease beyond this distance range (from an overdensity of a factor of 4 ± 1 to factors of 3 ± 1 and 2 ± 1). This suggests that the Virgo Overdensity extends farther out than previously known or, at least, that its stellar counts fade less sharply than in the case of colder streams. However, to what level the departure from the models at larger distances is due to remnants or influence of this substructure or due to the intrinsic structure of the smooth halo, can not be derived from the density profiles.

The two overdensities showing up in KiDS-South-15E and KiDS-South-15W are identified as the Sagittarius stream, based on the distances and locations recovered by 2MASS and the extrapolation from the SDSS-DR8 footprint. The overdensity in KiDS-South-15E starts to build up at $R_{GC} \approx 15$ kpc and peaks at $R_{GC} \approx 25$ kpc (with a factor of 2^{+3}_{-2}), decreasing slowly past the predicted distance of ~ 35 kpc and persisting at least out to 50 kpc (with a factor of 4 ± 2).

Table 3.5: Comparison between the best fit structural parameters found in this work for the combined KiDS + CFHT-INT data, the CFHT-INT data in Pila-Díez et al. (2015) and those reported by other groups in previous works. The different works have been labelled as follows: PD15 (Pila-Díez et al. 2015), J08 (Jurić et al. 2008), S11 (Sesar et al. 2011), D11 (Deason et al. 2011), R14 (Robin et al. 2014), dJ10 (de Jong et al. 2010), Ch01 (Chen et al. 2001), B08 (Bell et al. 2008), F14 (Faccioli et al. 2014), and S10 (Sesar et al. 2010a) and W09 (Watkins et al. 2009) as reanalysed in F14. The fitted models in F14, S10 and W09 have fixed oblateness and test two different values motivated by the previous findings in S11 and D11. This work, PD15, J08 and S11 use nearMSTO stars as a stellar tracer; D11 use A-BHB and A-BS stars; R14 and dJ10 use multiple stellar tracers; Ch01 and B08 use MSTO stars; and F14, S10 and W09 use RRLyrae stars as a tracer.

Work	dist. range (kpc)	χ^2_{red}	R_{br} (kpc)	n	n_{in}	n_{out}	q	w
CFHT-INT-broken	$[10, 60]$	1.5	19.5 ± 0.4	–	-2.50 ± 0.04	-4.85 ± 0.04	0.79 ± 0.02	–
KiDS-broken	$[10, 60]$	2.1	30.5 ± 0.5	–	-3.70 ± 0.05	-5.00 ± 0.05	0.81 ± 0.05	–
KiDS-CFHT-INT-triax.	$[10, 60]$	2.5	–	-4.26 ± 0.07	–	–	0.74 ± 0.04	0.94 ± 0.05
KiDS-CFHT-INT-broken	$[10, 60]$	2.4	$[22, 30)$	–	$[-3.30, -3.90)$	-4.6 ± 0.1	0.77 ± 0.05	–
J08	$[5, 15]$	$[2, 3]$	–	–	-2.8 ± 0.3	–	0.65 ± 0.15	–
S11	$[5, 35]$	3.9	27.8 ± 0.8	–	-2.62 ± 0.04	-3.8 ± 0.1	0.70 ± 0.02	excluded
D11	$[-, 40]$	–	27.1 ± 1	–	-2.3 ± 0.1	$-4.6^{+0.2}_{-0.1}$	$0.59^{+0.02}_{-0.03}$	–
R14	$[0, 30]$	–	–	-3.3 ± 0.1	–	–	0.70 ± 0.05	–
dJ10	$[7, 30]$	$[3.9, 4.2]$	–	-2.75 ± 0.07	–	–	0.88 ± 0.03	–
Ch01	$[-, 30]$	–	–	-2.5 ± 0.3	–	–	0.55 ± 0.06	–
B08	$[5, 40]$	2.2	~ 20	-3 ± 1	–	–	$[0.5, 0.8]$	≥ 0.8
F14	$[9, 49]$	0.8	28.5 ± 5.6	–	-2.8 ± 0.4	-4.4 ± 0.7	$q_{fix} = 0.70 \pm 0.01$	–
"	$[9, 49]$	1.04	26.5 ± 8.9	–	-2.7 ± 0.6	-3.6 ± 0.4	$q_{fix} = 0.59^{+0.02}_{-0.03}$	–
S10	$[9, 49]$	1.1	34.6 ± 2.8	–	-2.8 ± 0.2	-5.8 ± 0.9	$q_{fix} = 0.70 \pm 0.01$	–
"	$[9, 49]$	1.52	26.2 ± 7.4	–	-3.0 ± 0.3	-3.8 ± 0.3	$q_{fix} = 0.59^{+0.02}_{-0.03}$	–
W09	$[9, 49]$	1.1	27.6 ± 3.3	–	-2.5 ± 0.3	-4.3 ± 0.4	$q_{fix} = 0.70 \pm 0.01$	–
"	$[9, 49]$	0.69	26.9 ± 3.1	–	-2.1 ± 0.3	-4.0 ± 0.3	$q_{fix} = 0.59^{+0.02}_{-0.03}$	–

The overdensity(s) in KiDS-South-15E similarly extend from $R_{GC} \approx 15$ kpc out to 55 kpc, but displays a less strongly peaked distribution and, potentially, two possible crests. These residuals are less significant than those in KiDS-South-15E, with the highest overdensity level reaching a factor of 4^{+3}_{-2}.

A more extensive investigation of all overdensities (expected and unexpected), using additional tools other than stellar density profiles, is planned for a future publication.

3.5 Conclusions

In this work we have used deep wide-field images from the Kilo Degree Survey (KiDS) at VST to explore the stellar density profile of the halo. We have homogenized the PSF of our images in order to obtain more accurate fixed-aperture photometry and enhance the star- galaxy separation. The stellar completeness limit of our catalogues reaches $mag_r = 23.2$ mag. From these catalogues we have selected the near main sequence turnoff point stars (nearMSTO stars) as our stellar tracer for the shape of the halo using colour cuts in $g-r$ and $g-i$, magnitude cuts for faint stars in g, r, i and metallicity and absolute magnitude cuts on the $[Fe/H]$ and M_r estimators. This yields a subset of mainly halo F stars, significantly decontaminated from white-dwarf/M-dwarf pairs and quasars.

We have calculated the galactocentric distances of the nearMSTO stars through the photometric parallax method and used them to build density profiles along ten different lines of sights. We supplement these KiDS lines of sight with eight CFHT-INT lines of sight from our earlier study (Pila-Díez et al. 2015). We have fitted four galactic halo models to these data in order to derive insight on the stellar structure of the halo. For every fit we have masked out the profile sections where we anticipated stellar overdensities of accreted origin, in order to avoid biases on the structural parameters. Our best fits favour slightly a power law distribution with a break in the power law index ($\chi^2_{red} = 2.4$), closely followed by a single power law distribution with a mild triaxiality ($\chi^2_{red} = 2.5$).

Our best fit values for the break distance seem to be biased by the distribution of the data, favouring a value close to the transition between masked out and fitted data in the case of KiDS-only fits ($R_{break} = 30.5 \pm 0.5$ kpc), and favouring a value close to the start of our density profiles in the case of CFHT-INT-only fits and KiDS plus CFHT-INT fits ($R_{break} = 19.5 \pm 0.5$ kpc). This, in combination with a clear degeneracy of the inner power law index for the smaller break distance values and a disappearance of the degeneracy beyond 22 kpc, suggests that the real break distance is located somewhere $R_{break} \in [22, 30)$ kpc, in agreement with previous findings by other works.

We have found that the best fit value for the inner power law index strongly correlates with the break distance. Our data favour values for the inner and the outer indices on the steeper end of previous findings: $n_{in} = [-3.30, -3.90) \pm 0.05$ and $n_{out} = -4.6 \pm 0.1$, where previously most of the works suggested $n_{in} \in [-2.1, -3.3]$ and $n_{out} \in [-3.6, -5.8]$. As demonstrated in Pila-Díez et al. (2015),

the inclusion of large substructures such as the Sagittarius stream in halo fits can significantly influence the recovered parameters. Based on the exclusion of known substructure, together with the constraining power of our data at large distances, we conclude that the smooth outer stellar halo has a power law index close to -4.6.

We have found a disk axis ratio of $w = 0.94 \pm 0.05$, suggesting a very mild triaxiality. We do not test triaxiality in combination with the broken power law to avoid overparametrization problems. Few other works have reported on the triaxiality of the halo, and those who did agreed on $w > 0.8$. We have also found a polar axis ratio of $q = 0.77 \pm 0.05$, where most of the previous works found $0.55 \leq q \leq 0.70$ and some $q \leq 0.8$. Overall there seems to be a significant consensus on the stellar halo being moderately to quite oblate.

We have been able to recover a number of known stellar overdensities in our data-to-model residuals. Particularly, we clearly recover a strong signal matching the Sagittarius stream in the KiDS-North220E and KiDS-South-15E regions, a more moderate signal in KiDS-South-15W and a possible match (yet weak overdensity) in KiDS-North220W. Similarly, we recover overdensities matching the location and extent of the Virgo Overdensity in the KiDS-North180W and KiDS-North180E regions; in these two regions the overdensities seem to fade slowly, indicating either that the feature extends further out than previously thought or that it slowly blends with a smooth halo that does not exactly follow the models at these locations. Finally, we also seem to find overdensities in the already mentioned regions of KiDS-South-15E and KiDS-South-15W at further distances than those expected for the Sagittarius stream; this is suggestive of a previously unknown structure or a departure of the Sagittarius stream from the models. These overdensities will be further explored in future work, with tools more powerful than density profiles for characterizing substructure –such as Colour Magnitude Diagrams or matched filters–.